

AI-ASSISTED SUPER-RESOLUTION COSMOLOGICAL SIMULATIONS IV: AN EMULATOR FOR DETERMINISTIC REALIZATIONS

XIAOWEN ZHANG¹, PATRICK LACHANCE¹, ANKITA DASGUPTA², RUPERT A. C. CROFT¹, TIZIANA DI MATTEO¹, YUEYING NI³, SIMEON BIRD⁴ AND YIN LI⁵

¹ McWilliams Center for Cosmology, Department of Physics, Carnegie Mellon University, Pittsburgh, PA 15213

² Department of Astronomy and Astrophysics, Pennsylvania State University, University Park, PA 16802, USA

³ Harvard-Smithsonian Center for Astrophysics, 60 Garden Street, Cambridge, MA 02138, USA

⁴ Department of Physics and Astronomy, University of California Riverside

⁵ Department of Mathematics and Theory, Peng Cheng Laboratory, Shenzhen, Guangdong 518066, China

Version August 20, 2024

ABSTRACT

Super-resolution (SR) models in cosmological simulations use deep learning (DL) to rapidly supplement low-resolution (LR) runs with statistically correct, fine details. The SR technique preserves large-scale structures by conditioning on a low-resolution (LR) version of the simulation. On smaller scales, the generative deep learning (DL) process is stochastic, resulting in numerous possible SR realizations, each with unique small-scale structures. Validation of SR then relies on making sure that a specific statistic of interest is accurately reproduced by comparing SR and high resolution (HR) runs. In this study, we develop an emulator designed to reproduce the individual small-scale structures of an HR simulation as closely as possible. We process an SR realization alongside a specific High-Resolution Initial Condition (HRIC), transforming the SR output to emulate the results of a full simulation with that HRIC. By comparing visualizations, individual halo measures and cross-correlating Fourier modes we show that the emulated SR runs closely align with the corresponding HR simulation, even on length scales an order of magnitude smaller than the LR run. Additionally, small halos are trained to match the HR simulation, and the subhalo mass function is more accurately reproduced. These results show the promise of this method for generating numerous fast and accurate simulations and mock observations for large galaxy surveys.

1. INTRODUCTION

Cosmological N-body simulations have served as powerful computational tools since the 1960s (von Hoerner 1960; Aarseth 1963) for solving the non-linear dynamics intrinsic to cosmic structure formation. High-resolution (HR) simulations employing state-of-the-art, massively-parallel codes, such as MP-Gadget, evolve a large number of particles under gravity, tracking the formation of structures on the order of galaxy size and larger. These simulations demand significant time and computational resources, forcing researchers to make trade-offs between resolution and size of simulation volumes. Hydrodynamic simulations, such as Illustris-TNG (Springel et al. 2018), SIMBA (Davé et al. 2019) and ASTRID (Bird et al. 2022; Ni et al. 2022), which model the baryonic matter as a separate component, require even more computational investment compared to gravity-only N-body simulations. Consequently, researchers are often compelled to reduce resolution due to the intensive computational demands or, alternatively, select smaller volumes to allow for finer scales. For example, the small volume high-resolution FIRE suite (Hopkins et al. 2014) and the ABACUS summit (Maksimova et al. 2021) runs optimized for large-scale structure. In the present paper we explore the use of Machine Learning (ML) techniques (Yue et al. 2016) to sidestep these limitations by vastly accelerating simulations by many orders of magnitude. We anticipate that these hybrid N-body-ML simulations will make certain

tasks much easier (e.g., making mock catalogs for large galaxy surveys).

In recent years, ML has become a promising tool for physicists, particularly the use of Deep Learning (DL) (Dvorkin et al. 2022). ML models have been developed to predict different baryonic properties from dark matter-only simulations, including the galaxy distribution (Modi et al. 2018; Zhang et al. 2019), the tSZ effect (Tröster et al. 2019), the 21 cm emission distribution (Wadekar et al. 2020), and stellar maps (Dai & Seljak 2021). Predictions of nonlinear structure from linear cosmological initial conditions (He et al. 2019; Berger & Stein 2019; Bernardini et al. 2020; Alves de Oliveira et al. 2020) and from the dark matter density field (Kodi Ramanah et al. 2020a) have proved that DL based Neural Networks (NNs) can capture highly nonlinear structures. Training large NNs requires extensive, high-quality datasets. CAMELS (Cosmology and Astrophysics with Machine Learning Simulations, Villaescusa-Navarro et al. 2020), a large-scale project with a training set of over 4000 hydrodynamical simulations run with different hydrodynamic solvers and subgrid models for galaxy formation. A prime purpose of this set is to investigate the interplay of baryonic effects and cosmology, using machine learning techniques.

In a quest to achieve faster results comparable in accuracy to full HR N-body simulations, researchers have applied "Super-Resolution" (SR) techniques to lower resolution cosmological simulations (see e.g., Li et al. 2021 and other papers in this series). SR in general describes the situation where information

is added below the resolution scale of initially Low Resolution (LR) data such as a photograph (e.g., in [Johnson et al. 2016](#)) to create an HR version. However, SR remains a challenging and ill-posed problem in ML, because an infinite number of HR results can be downsampled to the same LR input, meaning the SR model learns a conditional probabilistic distribution of HR simulations based on a single LR simulation. This ‘one-to-many’ regime can be useful when many simulations or mock observations are needed for accurate and precise cosmological parameter inference. It can however make validation difficult, as it can only be done in a statistical sense by averaging over ensembles.

Generative Adversarial Network (GAN) ([Goodfellow et al. 2014](#)) architectures have already proven to be effective in SR tasks ([Wang et al. 2019](#)) and have been applied to the generation of 2D images of cosmic webs ([Rodríguez et al. 2018](#)), 3D matter density fields ([Perraudin et al. 2019](#)) and cosmological mass maps ([Perraudin et al. 2020](#)). GANs consist of two separate NNs: a generator, which generates candidates, and a discriminator, which provides feedback by comparing real data with generated candidates. In previous work, an SR framework which applies a GAN approach directly to N -body simulation particles has been explored, covering from displacement only ([Li et al. 2021](#)) to full 6-D phase space ([Ni et al. 2021](#)), and which can also conditioned on redshift ([Zhang et al. 2023](#)) (hereafter Paper I, Paper II and Paper III). The output of this framework can be treated and analyzed in the same manner as full N -body simulation data. The same framework has also been used for a fuzzy dark matter cosmology ([Sipp et al. 2023](#)). In Paper I, II and III, we trained our GAN based framework to perform a stochastic mapping from LR input to SR output, where stochasticity is injected during the generation process. These models aim to learn a probability distribution of HR outputs conditioned on LR inputs. By sampling this distribution using a special technique, as described in [Zhang et al. \(2023\)](#), we can carefully control the randomness in the SR field, allowing us to generate simulations with outputs at any redshift desired. Instead of checking that summary statistics of the SR model are within expected bounds, an SR run that reproduces the individual structures of the HR run would (at least down to some length or mass scale) be a valid cosmological simulation, one that could be used to compute any summary statistic. This is one of the goals of this paper.

Recently, denoising diffusion models ([Sohl-Dickstein et al. 2015](#); [Ho et al. 2020](#)) have become state-of-the-art, outperforming GANs for some image generation tasks and also being used in SR. It has been shown that super-resolving a 3D density field conditioned on an LR density field ([Rouhiainen et al. 2023](#)) using a diffusion model has comparable performance to GAN results and does not suffer from unstable training and mode collapse. Several approaches employing diffusion models demonstrate the potential of this method, such as in 2D galaxy images ([Smith et al. 2022](#)) and in 2D simulations ([Schanz et al. 2023](#)) using filter-boosted tricks. However, their work is limited to 2D cases only.

In this work, we introduce an emulator framework which can adjust the SR outputs to their HR counterparts by conditioning on specific high-resolution initial conditions (HRICs). These specific HRICs have the same large-scale modes as the LR N -body simulations that are used to generate SR outputs. Other studies have employed emulators, such as [Kodi Ramanah et al. \(2020b\)](#), which combines LR and HRICs for super-resolution tasks on 3D density fields. Notably, no stochasticity is in-

jected into the model, similar to our approach. Additionally, [Jamieson et al. \(2023\)](#) uses a neural network to map the linear approximation at $z = 0$ to real N -body simulations with various cosmological parameters, using a Lagrangian description. To achieve accurate SR emulation of the HR simulations down to small-scales, we find that using adversarial training techniques are crucial for correcting small-scale discrepancies. We explore emulators trained with this technique (hereafter referred to as “Emulator”), and compare them with our previous work in [Zhang et al. \(2023\)](#) (hereafter referred to as “SR”).

The paper is structured as follows. In Section 2, we discuss the generation of data sets and summarize the details of our neural networks and the training process. In Section 3 we show the performance of our emulator, specifically visual validation in 3.1, Fourier mode cross-correlations in 3.2 and halo catalog in 3.3. In Section 4, we discuss our findings, and we summarize our results and conclude in Section 5. We have also included the results of training without discriminator guidance in Appendix A.

2. METHOD

2.1. Dataset

The N -body simulation is a widely used tool for understanding the nonlinear evolution of cosmic structures. Given a fixed set of cosmological parameters (in this work, we use the WMAP9 cosmology, as prescribed by [Hinshaw et al. 2013](#)), this method involves dividing the mass distribution into N equal-mass particles. We run both LR and HR simulations using MP-Gadget¹, a highly parallel code that solves the gravitational force using the TreePM method ([Bagla 2002](#)). Long-range forces are calculated on a particle mesh in Fourier space, and short-range forces are computed through a hierarchical tree structure. Our LR and HR simulation tasks follow the Lagrangian description, with particles are tracers of both displacement and velocity fields. The displacement of an individual particle is:

$$\mathbf{d}_i = \mathbf{x}_i - \mathbf{q}_i \quad (1)$$

where \mathbf{d}_i is the displacement of i th particle, \mathbf{x}_i is the current position and \mathbf{q}_i is its initial position on the uniform grid. Similarly, the velocity of individual particle is :

$$\mathbf{v}_i \equiv \dot{\mathbf{x}}_i = \dot{\mathbf{d}}_i, \quad (2)$$

where the dots denote time derivatives. The initial conditions for our simulations are generated at $z = 99$ using a power spectrum calculated by CLASS ([Lesgourgues 2011](#)). First-order Lagrangian perturbation theory ([Zel’dovich 1970](#); [Crocce et al. 2006](#)) is used to initialize particle positions and velocities. The definition of initial displacement $\mathbf{d}_{init,i}$ and velocity $\mathbf{v}_{init,i}$ for particles is similar to Eq. 1 and 2. Cosmological parameters follow the WMAP9 cosmology ([Hinshaw et al. 2013](#)), with matter density $\Omega_m = 0.2814$, dark energy density $\Omega_\Lambda = 0.7186$, baryon density $\Omega_b = 0.0464$, power spectrum normalization $\sigma_8 = 0.82$, spectral index $n_s = 0.971$, and Hubble parameter $h = 0.697$. The mean spatial separation of the dark matter particles is used to determine the gravitational softening length, which is set to $1/30$ of this value. Our training dataset is comprised of 8 dark matter only simulations, each with LR and HR simulation pairs. Each LR-HR simulation pair has 64^3 and 512^3 particles, respectively, with box size $100h^{-1}\text{Mpc}$. The mass resolution is $m_{\text{DM}} = 2.98 \times 10^{11} h^{-1} M_\odot$.

¹ <https://github.com/MP-Gadget/MP-Gadget>

for LR, and $m_{\text{DM}} = 5.8 \times 10^8 h^{-1} M_{\odot}$ for HR. Each pair has a unique random seed for its initial condition, so the initial conditions differ for eight simulations. In addition, we also create a test dataset with 3 LR and HR simulation pairs. Each pair consists of 60 snapshots from $z = 1$ to $z = 0$, with the same cosmological parameters as the training set but different initial condition random seeds. During data pre-processing, we first divide the particle displacement and velocity fields into cubical chunks. We then concatenate the displacement field and velocity field channel-wise since they share the same spatial resolution. This process is applied similarly to the HRICs.

2.2. Model Architecture and General Training Process

U-Net is a universal architecture that was first designed for semantic segmentation (Ronneberger et al. 2015). It consists of an encoder and a decoder, with a bottleneck between them. The encoder progressively downsamples the input towards the bottleneck, while the decoder upsamples the data from bottleneck back to the original resolution. "Skip-connections" link the encoder and decoder at corresponding resolutions. U-Nets have also been applied to super-resolution/style transfer tasks (Johnson et al. 2016), image to image translation, image uncropping and more (see discussion in Saharia et al. 2021, for a review). Recent diffusion models (Sohl-Dickstein et al. 2015; Ho et al. 2020) also use U-Nets for denoising.

The lower panel of Figure 1 illustrates the detailed architecture of our U-Net model. The encoder part extracts features from the input and downsamples them towards the bottleneck. This forces the model to learn the key information from the input and embed it into a low-dimensional space. Starting from the input resolution, the decoder downsamples the learned feature until it reaches the bottleneck blocks. Each decoder block at the same resolution consists of two residual blocks. We follow BigGAN's (Brock et al. 2018) residual block structure since it has been proven to have good performance and can be scaled to different depths. All residual blocks contain two branches, one "skip" branch with a 3D size 1 convolutional block, the other "main" branch, which first normalizes the input with Group Normalization (Wu & He 2018), then passes through a Sigmoid Linear Unit (SiLU) activation function (Elfwing et al. 2017). The second group normalization layer is applied to normalize the output from a 3D size 3 convolutional block. Finally, after one more activation function and one 3D size 3 convolutional block, the output from the "main" branch is added to the output from the "skip" branch. The Up/Down layer denotes the upsampling or downsampling procedure, only applied in *Res Up/Down Blocks*. The decoder part decodes and upsamples the features from the bottleneck and the "skip" connections from the encoder. The information from the encoder is passed to the decoder at multiple resolution levels, to maintain information at different levels and avoid vanishing gradient issues. No stochasticity is injected in this model.

The goal of our model is to adjust the fields output by a stochastic SR model to those that corresponds as exactly as possible to the output of a specific HR simulation by conditioning on the HRICs. Due to the limitations of GPU memory, we first split the SR field and HRICs into equal size chunks, then concatenate them in a channel-wise fashion since they have the same spatial dimensions. Both chunks pass through the encoder, bottleneck and decoder steps together, and are then compared to the real HR simulations generated from the same HRICs. To evaluate our emulator's output, we use the

Charbonnier loss function (Barron 2017), which is defined as

$$L_{\text{Charbonnier}}(x, y) = \sqrt{(x - y)^2 + \epsilon^2} \quad (3)$$

Here, ϵ acts as a hyperparameter regulating the tolerance of the loss function. We evaluate our output simulation using a combination of multiple objective functions. The simplest loss function aims to minimize the errors in the displacement and velocity fields in a Lagrangian description:

$$\mathcal{L}_{\text{Lag}} = L_{\text{Charbonnier}}(\mathbf{d}_{\text{output}}, \mathbf{d}_{\text{HR}}) \quad (4)$$

In Papers I, II and III, we have shown that adding Eulerian density field information greatly improves the model performance. Hence, we calculate $n(\mathbf{x})$, which is the particle number in voxel \mathbf{x} , using a CIC scheme. The second term in our loss function is

$$\mathcal{L}_{\text{Eul}} = L_{\text{Charbonnier}}(n(\mathbf{x})_{\text{output}}, n(\mathbf{x})_{\text{HR}}) \quad (5)$$

Using feedback from discriminator (i.e. adversarial loss) is common in image generation and image to image translation tasks. It is used to enhance perceptual quality of the output. We use the same definition of adversarial loss \mathcal{L}_{Adv} as in previous SR works. The total loss for our emulator network is:

$$\mathcal{L}_{\text{total}} = \mathcal{L}_{\text{Lag}} + \mathcal{L}_{\text{Eul}} + \lambda \mathcal{L}_{\text{Adv}} \quad (6)$$

The parameter λ is a weight to balance the contribution of the different loss terms, and the value of λ is set empirically to 3×10^{-2} . We have settled on this value after experimentation to balance the accuracy and perceptual quality of the outputs.

2.3. Training Specifics

We set the base channel of our U-net to 64, with channel multipliers at different resolutions set to [1, 1, 2, 2]. For the discriminator network, the base channel is 32 and the channel multipliers at each resolution are [1, 2, 4, 8]. The Eulerian field, sampled on meshes of side length 1024 cells, is concatenated with a 6D field of particle displacements and velocities, serving as the input for our discriminator. Data augmentation techniques are applied, including random flips along three different axes and random shifts of the chunk crop position. We use Rectified Adam (Liu et al. 2019) in training to avoid identified convergence problem suffered by the Adam optimizer. We set parameters $\beta_1 = 0.9$ and $\beta_2 = 0.999$ which is the default in Pytorch (Paszke et al. 2019). The batch size is set to 1 which is the largest size possible given our setup. Training was conducted using NVIDIA A100 GPUs.

3. RESULTS

We now compare the outputs of our emulated SR simulations with full N-body HR runs. In our previous work on stochastic SR simulations (Li et al. 2021; Ni et al. 2021; Zhang et al. 2023), we compared the results using various summary statistics, including power spectra and halo mass functions. In the current work, because we are emulating the exact HR fields, we can perform comparisons on an individual basis rather than relying solely on statistical measures. Consequently, we supplement our analyses with additional approaches, such as visual comparisons of individual structures and cross-correlation of the individual Fourier modes between the emulated and HR runs. We also perform comparison at the halo level with the corresponding HR simulation.

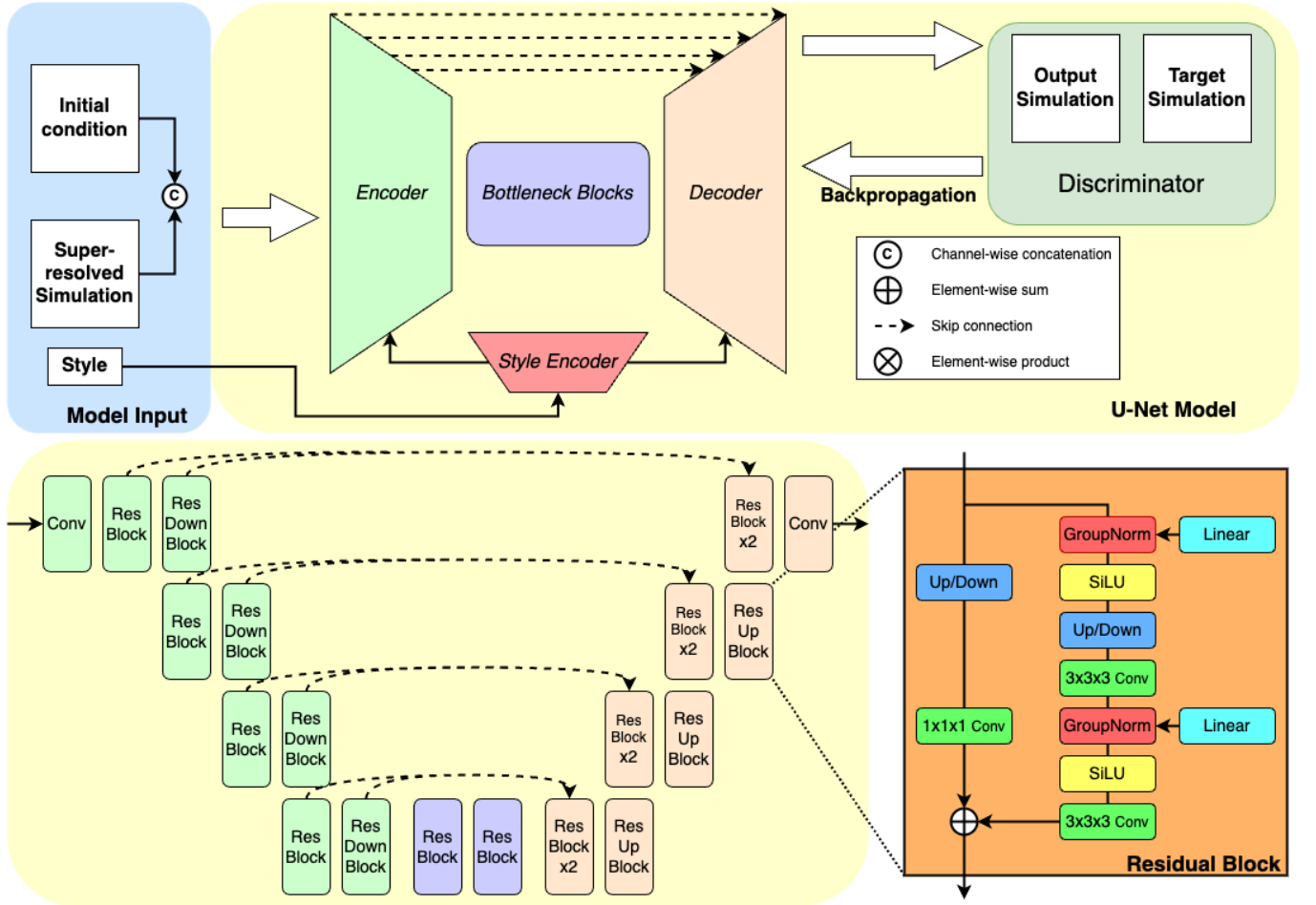


FIG. 1.— **Upper Panel**: Schematic plot of the main components of the model and the entire training process. **Lower Panel**: Architecture of our U-Net model and detailed structure of our Residual Block. The *Res up Block* or *Res Down Block* blocks correspond to the up-sampling or down-sampling blocks in the detailed structure, while the *Res Blocks* do not have up/down sampling blocks.

3.1. Visual comparison

For our initial validation, we visually analyze the differences between the HR fields obtained from N -body simulations and the SR fields of our SR model, as well as the output from our newly designed Emulator Neural Network. Figures 2 and 3 present three-dimensional visualizations of dark matter density plots, generated by projecting all particles contained within the box. The images are rendered using the `gaepsi2` code.² The first row shows the whole $(100h^{-1}\text{Mpc})^3$ volume, centered on several massive halos, to show the large-scale structures, the second row and the third row shows a sub-volume of $(20h^{-1}\text{Mpc})^3$ and $(11h^{-1}\text{Mpc})^3$, respectively, to illustrate finer details and halo distributions.

The visual representation of the density fields reveals that both our SR model and emulator are capable of generating large-scale structures appearing morphologically similar to one another. Regarding the small scales, the SR model produces visually authentic features based on the constraint from the LR input, with the fine details appearing reasonable. Our Emulator refines these small-scale details to better match the HR by conditioning on the HRICs. The SR model successfully forms halos in regions where the LR input lacks resolution, while the Emulator further adjusts their positions to align with the HR simulation. As an example, as shown in the bottom

row of Figure 3, the SR field generates a series of halos lying along a thin filament, and the emulator adjusts the field to align with the HR field, placing three massive halos at the center of the box.

3.2. Fourier analysis: cross-correlation of individual modes

The over-density field at position x , is defined as

$$\delta(x) = \frac{\rho(x) - \bar{\rho}}{\bar{\rho}} \quad (7)$$

Where $\rho(x)$ is the density at position x and $\bar{\rho}$ is the average density. The Fourier transform is used to compute the density modes $\delta(k)$, and hence the usual matter power spectrum is given by:

$$\langle \delta(\mathbf{k}) \delta(\mathbf{k}') \rangle = (2\pi)^3 \delta^3(\mathbf{k} + \mathbf{k}') P(k) \quad (8)$$

Here $\delta^3(\mathbf{k} + \mathbf{k}')$ denotes the 3D Dirac delta function. The Nyquist frequency is $k_{\text{Nyq}} = \pi N_{\text{mesh}}/L_{\text{box}}$. In our test set, $N_{\text{mesh}} = 512$ and $L_{\text{box}} = 100h^{-1}\text{Mpc}$.

We quantify the difference between the SR prediction and the true HR simulation by calculating the cross-correlation coefficient of individual modes in Fourier space:

² <https://github.com/rainwoodman/gaepsi2>

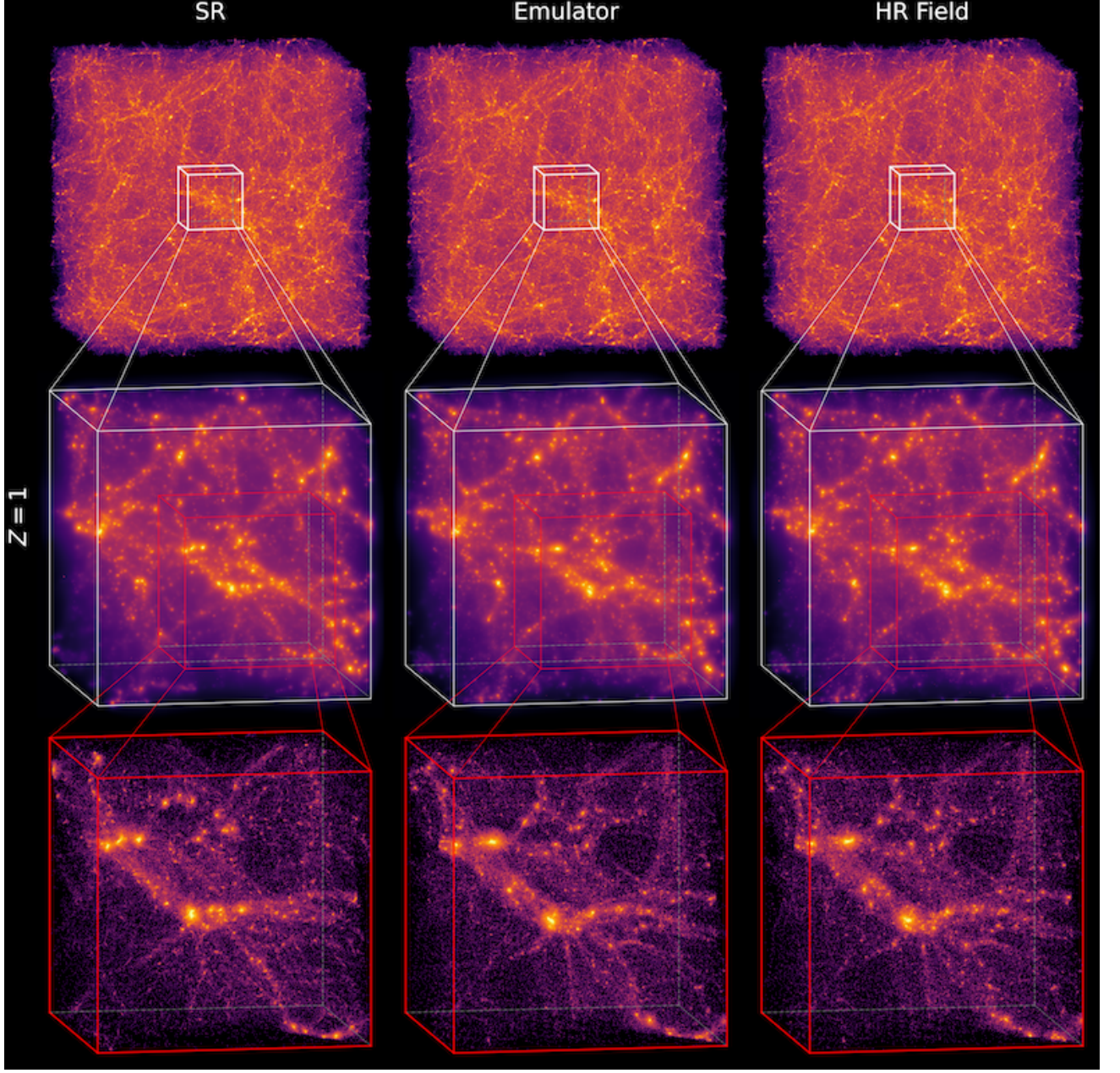


FIG. 2.— 3D visualization of the SR, Emulator, and HR dark matter density fields with boxsize $100h^{-1}\text{Mpc}$ (first row), $20h^{-1}\text{Mpc}$ (second row), $11h^{-1}\text{Mpc}$ (third row) at $z = 1$.

$$r(k) = \frac{\langle \delta_{\text{pred}}(\mathbf{k}) \delta_{\text{true}}(\mathbf{k}') \rangle}{\sqrt{\langle \delta_{\text{pred}}(\mathbf{k}) \delta_{\text{pred}}(\mathbf{k}') \rangle \langle \delta_{\text{true}}(\mathbf{k}) \delta_{\text{true}}(\mathbf{k}') \rangle}} \quad (9)$$

$$= \frac{P_{\text{pred,true}}(k)}{\sqrt{P_{\text{pred,pred}}(k) P_{\text{true,true}}(k)}}, \quad (10)$$

where $\delta_{\text{pred}}(\mathbf{k})$ is the predicted density field constructed from the emulator, and $\delta_{\text{true}}(\mathbf{k})$ is the density field constructed from the real HR N-body simulations. Here, $r(k)$ measures the correlation between the phases of the modes of the two fields. In an ideal scenario, where the true and predicted fields are perfectly correlated, the cross-correlation between the two fields would be 1 across all scales. The stochasticity is defined as $1 - r^2(k)$, which quantifies the variation in the prediction

that cannot be accounted for by the HR simulations.

To quantify agreement of the velocity field, we examine the momentum in Fourier space. The momentum field $p(x)$ is defined as momentum at position x . This is calculated using the same CIC scheme as the matter density field. The Eulerian momentum power spectrum is given by:

$$\langle p(\mathbf{k}) p(\mathbf{k}') \rangle = (2\pi)^3 \delta^3(\mathbf{k} + \mathbf{k}') P_{\text{momentum}}(k) \quad (11)$$

The momentum cross-correlation coefficient is calculated using the analogous equation to Eq. 10. Since each particle is initially assigned to a uniform grid with the same number of cells as our density and momentum field, we can also work with the displacement field in Fourier space. The displacement power spectrum (on the initial grid) is given by:

$$\langle d(\mathbf{k}) d(\mathbf{k}') \rangle = (2\pi)^3 \delta^3(\mathbf{k} + \mathbf{k}') P_{\text{displacement}}(k) \quad (12)$$

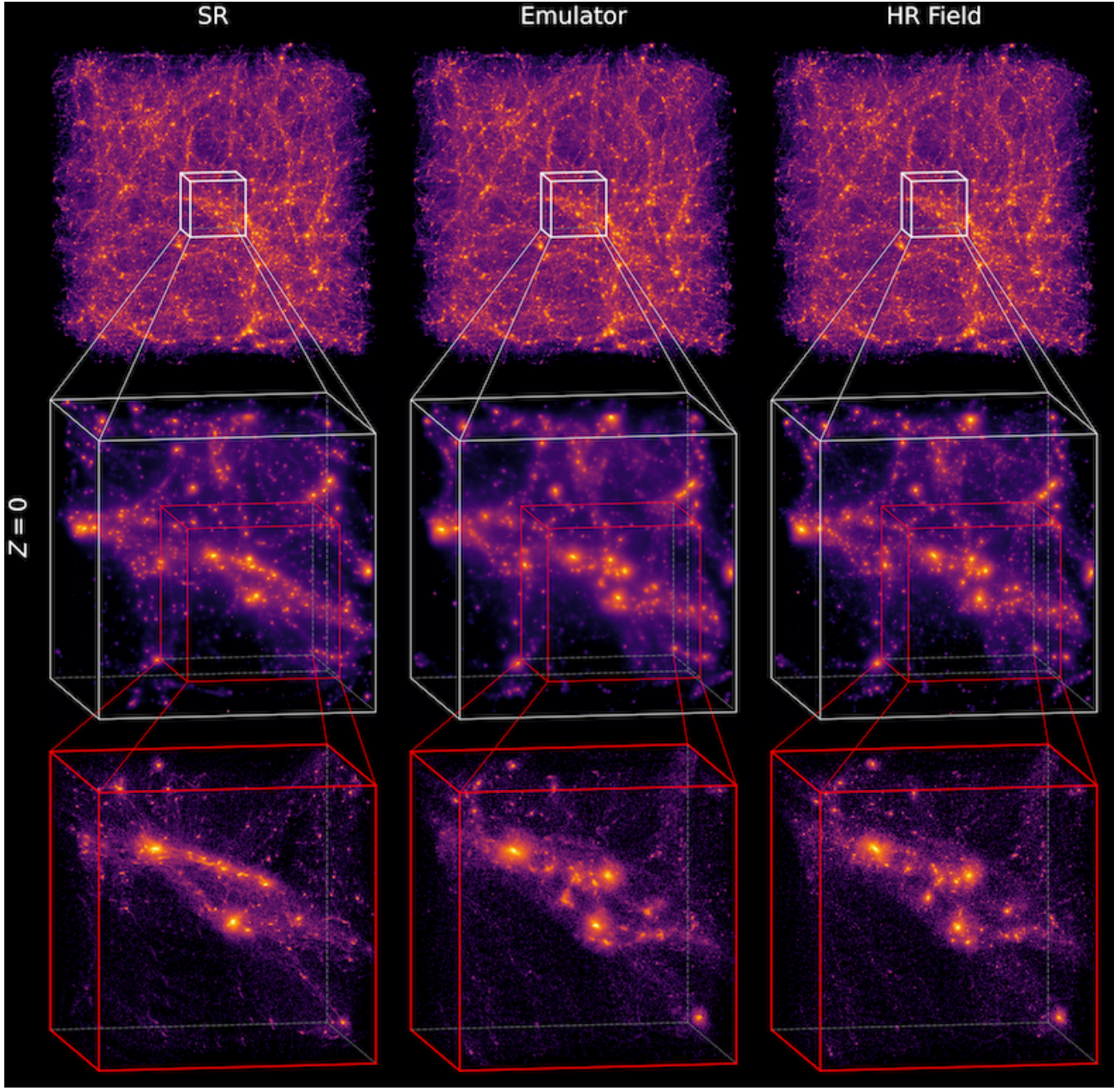


FIG. 3.— 3D visualization of the SR, Emulator, and HR dark matter density fields with boxsize $100h^{-1}\text{Mpc}$ (first row), $20h^{-1}\text{Mpc}$ (second row), $11h^{-1}\text{Mpc}$ (third row) at $z = 0$.

We use the same definition as Eq. 10 for the cross-correlation. The results are plotted in Figure 4, with the color of each curve representing the redshift of its corresponding simulation. We select 5 snapshots from each simulation at redshift $z = 1, 0.8, 0.5, 0.2, 0$.

The results of the density power spectrum error are presented in the top row of Figure 4. The outputs of the Emulator model are considerably more accurate than those of the SR model. At $k = 1 h \text{ Mpc}^{-1}$, which is around the LR Nyquist frequency, the SR density field deviates from the HR model by exhibiting 7% stochasticity, whereas our emulator maintains less than 2% across all redshifts. The discrepancy between the SR and HR fields increases to over 99% stochasticity at $k = 8.5 h \text{ Mpc}^{-1}$, but the Emulator significantly reduces this to around 50%. The error at the HR Nyquist frequency is also reduced from 100% for SR to between 55-80% in the Emula-

tor's output, depending on redshift. A significant fraction of the structures are reproduced even even at $k = 10 h \text{ Mpc}^{-1}$ and beyond. The second and third rows show the error in the displacement and momentum power spectra, respectively. We observe significant improvements in accuracy with the Emulator model. The displacement power spectrum error in the SR simulation, which is around 60%, is reduced to less than 10% by our Emulator. Regarding the momentum power spectrum error, the Emulator reduces the SR simulation's error from 40% to less than 5%.

In the Emulator panel for the stochasticity of the density modes, we display another blue dashed line. This represents the results of the Emulator trained on a single redshift ($z = 0$). This version shows a significant improvement compared to the multiple-redshift model, reducing the error at the HR Nyquist frequency to around 12%, and the error at $k = 10 h \text{ Mpc}^{-1}$

to only 5%. These results represent the best that the emulator is able to achieve, but we have not been unable so far to reproduce this accuracy when the emulator is trained for multiple redshifts. While our emulator in its current state is aiming for use cases currently carried out by approximate methods, it is interesting to note that a 5% error in Fourier space at $k = 10 \ h \text{ Mpc}^{-1}$ is comparable to many full N-body simulation codes (see e.g., Figure 14 of Heitmann et al. 2008).

We can ask what limits the emulator's accuracy, and how this can be improved: the movements of particles within a virialized halo are rapid and can vary significantly over time. This high frequency behavior diminishes the emulator's ability to accurately match the positions and velocities of particles at the individual level. This task is challenging because the HRICs do not contain information within non-linear regimes. Additionally, due to memory constraints, the full simulation must be split into chunks, with the GPU handling a maximum of 128^3 particles per chunk. A single large halo may span multiple chunks, meaning the emulator lacks access to all the relevant particle information. This limitation could be mitigated by using a GPU with more memory or use a more memory efficient model. Despite this, the Emulator demonstrates strong performance, effectively adjusting the small-scale details generated by the SR model starting from $k = 1 \ h \text{ Mpc}^{-1}$, achieving excellent accuracy up to the Nyquist frequency of the initial grid. It also maintains decent accuracy up to $k = 10 \ h \text{ Mpc}^{-1}$.

3.3. Halo catalog analysis

Dark matter, under gravitational clustering, forms high-density virialized structures and local maxima within them, known as halos and subhalos. Understanding these structures and substructures that potentially host galaxies is crucial for connecting theoretical models to observations. These halos and subhalos, identified using halo finder algorithms, play a key role in constructing mock observational catalogs from N-body simulations. We use the SUBFIND code (Springel et al. 2001) to determine the positions and masses of halos and subhalos, as well as to build merger trees. SUBFIND identifies substructures by detecting locally dense and gravitationally bound groups of particles. It starts with the Friends-of-Friends algorithm, followed by the estimation of each particle's local density via adaptive kernel estimation.

We employ the SUBFIND algorithm on test sets of SR output, Emulator output and HR output of the N -body simulation and compare statistical properties of the halo and subhalo populations. Throughout this work, we examine halos and subhalos with at least 100 tracer particles in our test sets.

3.3.1. Host and subhalo abundance

The most straightforward comparison involves counting the number of halos as a function of mass. The halo mass function is defined as:

$$\Phi = dn/d \log_{10} M_h, \quad (13)$$

where dn is the comoving number density of halos within an infinitesimal logarithmic mass bin $d \log_{10} M_h$, and the fractional error is calculated using:

$$\text{error} = \frac{\Phi_{\text{Pred}}}{\Phi_{\text{HR}}} - 1. \quad (14)$$

Figure 5 and Figure 6 show the mass function for host halos and subhalos measured from the SR, Emulator, and HR field

test sets across five redshifts from $z = 1$ to $z = 0$. The colors of the curves represent the redshift of each simulation, with shaded regions indicating the 1σ standard deviation. In Figure 5, we present host halo mass function in the top panel and its fractional error in the bottom panel. In Figure 6 we show the subhalo mass function in the same format.

For host halos, we observe that the Emulator is slightly less accurate than the SR model within the lower mass region, particularly at $z = 0$. Regarding substructures, Figure 6 shows that our Emulator model statistically improves over the SR model in the mass range covering $[10^{11}, 10^{13}] M_\odot$. The SR model exhibits an approximately 90% deficit in the subhalo mass function at the lower mass end, whereas our Emulator significantly reduces this error by at least 50%.

Figure 7 shows the mean occupation number of subhalos as a function of the host halo mass. The SR field has an overall offset from the HR value, with from 50% – 90% fewer subhalos being predicted per halo than in the HR simulation. The emulator improves on this from the lower mass end up to $10^{13} M_\odot$, reducing the error to between 16% and 75%. As shown in Figure 8, the SR output fails to accurately predict the correct subhalos. However, our emulator model successfully predicts the correct number of subhalos with similar relative positions.

Both the SR model and the emulator predict fewer subhalos within the most massive halos. We believe that this is partly due to the limited Eulerian field resolution within our discriminator. With the current setup of 512 mesh cells along each side of a $100h^{-1}\text{Mpc}$ box, the resolution per Eulerian field "pixel" is approximately $0.2h^{-1}\text{Mpc}$, limiting the discriminator's ability to detect real substructures within massive halos. Increasing the resolution by a factor of f would expand the Eulerian field by a factor of f^3 , demanding more GPU memory. Despite these challenges, our emulator remains quite successful at predicting substructures. Across the halo mass range from $10^{11} - 10^{15} M_\odot$, the mean number of subhalos per halos varies by three orders of magnitude, with the emulator providing relatively accurate results.

We discover that some halos are divided between simulation chunks that are processed separately. This occurs during both the training and testing phases and causes the model to lack complete halo information. That this occurs is due to GPU memory constraints which requires the simulation to be broken up into relatively small chunks. To quantify the effect of this, we select halos where 99% of their particles are contained within the same chunk. The blue dashed line in the lower panel of the Emulator illustrates the result, showing 10% improvement in the error margin at approximately $10^{11} M_\odot$. This highlights the significance of the chunking issue in the SR+Emulator procedure. The problem could be mitigated by using a more memory-efficient model or by splitting the model sequentially across multiple GPUs for training and testing.

3.3.2. Halo cross correlations

Our emulator not only refines the SR field but also corrects the positions and velocities of particles, ensuring that the masses and positions of halos are consistent with their counterparts in the HR test sets. To evaluate the accuracy of halo positions and masses, we introduce a new statistic called the "halo cross spectrum". This metric is similar to the cross-correlation coefficient of individual Fourier modes described in Section 3.2, but it focuses on halo masses and positions. In this method, each halo is treated as an individual particle, and

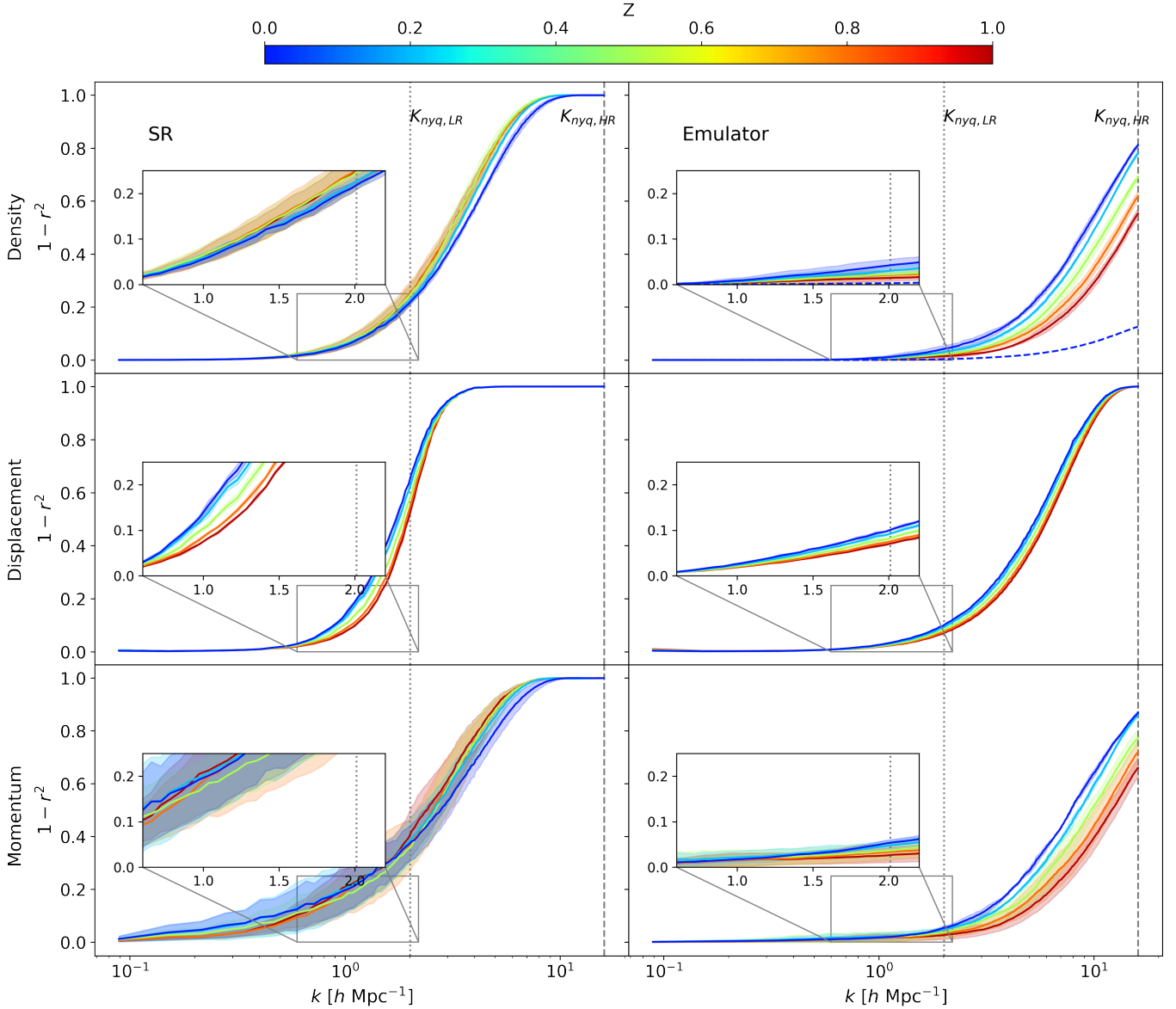


FIG. 4.— Stochasticity, derived from the correlation coefficient of individual Fourier modes as a function of wavenumber. From left to right, we present results for the cross-correlation of HR (the true N-body simulation) with SR and the Emulator output. The color of each curve corresponds to the redshift, as indicated by the color bar. The shaded area shows the 1σ standard deviation from all test sets. The vertical dotted gray line is the Nyquist frequency of the LR simulation and the dashed gray line indicates the Nyquist frequency of HR simulation. The blue-dashed line in the top right panel shows the result for a version of the emulator trained on a single redshift ($z = 0$, see text).

assigned to a 512^3 mesh grid using the Cloud-in-Cell (CIC) scheme, with the mass of each particle corresponding to the halo mass. We then perform a Fourier transform on the mesh and deconvolve the CIC window function to obtain the Fourier modes $h(\mathbf{k})$. The power spectrum $P_h(k)$ in this case is:

$$\langle h(\mathbf{k}) \cdot h(\mathbf{k}') \rangle = (2\pi)^3 \delta^3(\mathbf{k} + \mathbf{k}') P_h(k) \quad (15)$$

The cross-correlation coefficient of individual modes is calculated using the same method applied to the matter density in Section 3.2. The results are plotted in Figure 9.

Figure 9 shows the halo stochasticity error. We find that the emulator achieves smaller errors than the SR model across all mass ranges. In the mass range greater than $10^{13} M_\odot$, the improvements made by Emulator are less significant compared to the enhancements within the mass range of $[10^{11}, 10^{13}] M_\odot$. This is because our SR model, being conditioned on LR simu-

lations, already constrains the positions and masses of massive halos. The emulator fine-tunes these positions and masses to more closely match those in the HR field test set. Since the SR model conditions its predictions on LR simulations, it is expected that the correlation between the SR field and the HR field diminishes from $10^{13} M_\odot$ down to $10^{11} M_\odot$. However, by adjusting halos based on the HRICs, our emulator achieves much higher accuracy within this mass range. In the mass regime below $10^{11} M_\odot$, the HRICs lack sufficient information on less massive halos, resulting in both the SR field and emulator output failing to predict halos that match the positions and masses of those in the HR field.

3.3.3. Merger histories

Given the emulator's success in reproducing the positions and masses of individual halos, it is interesting to examine

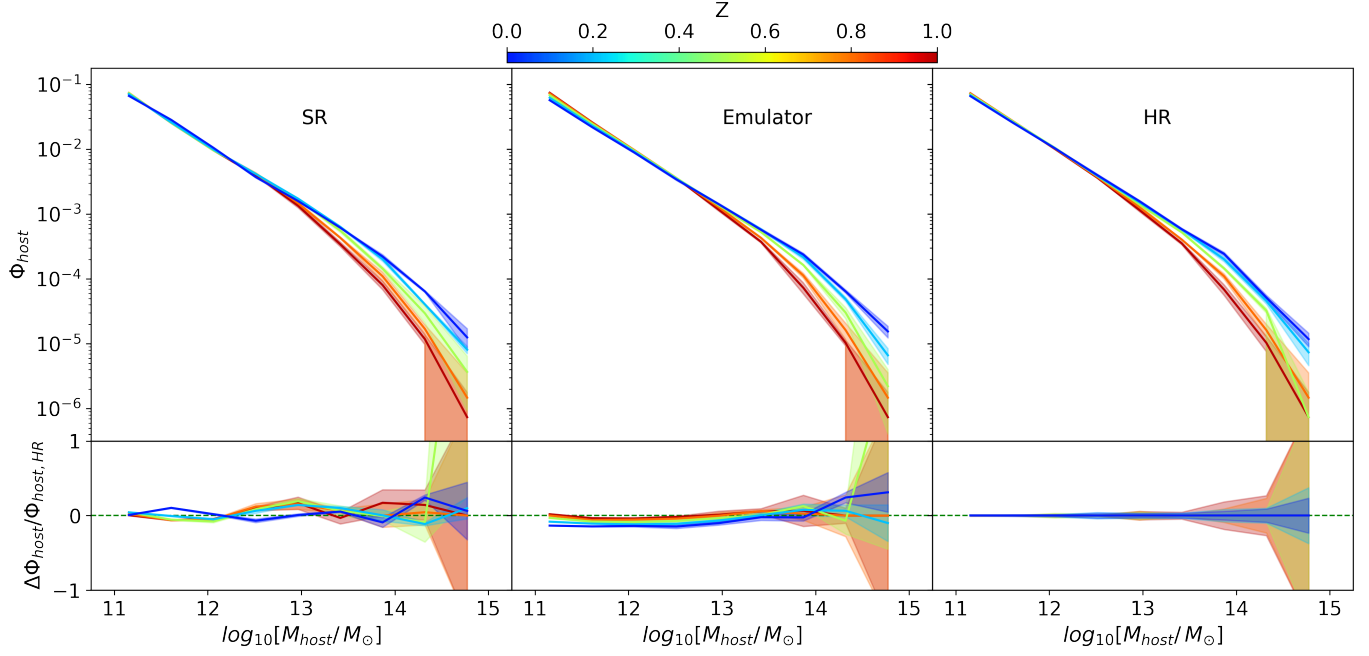


FIG. 5.— The host halo mass function at redshifts $z = 1, 0.8, 0.5, 0.2, 0$ measured from the SR, Emulator and HR fields. The color of each curve denotes the redshift of simulation in test set. The shaded areas indicate 1σ standard deviation from all test sets. The upper panel shows halo mass functions and lower panel shows fractional errors.

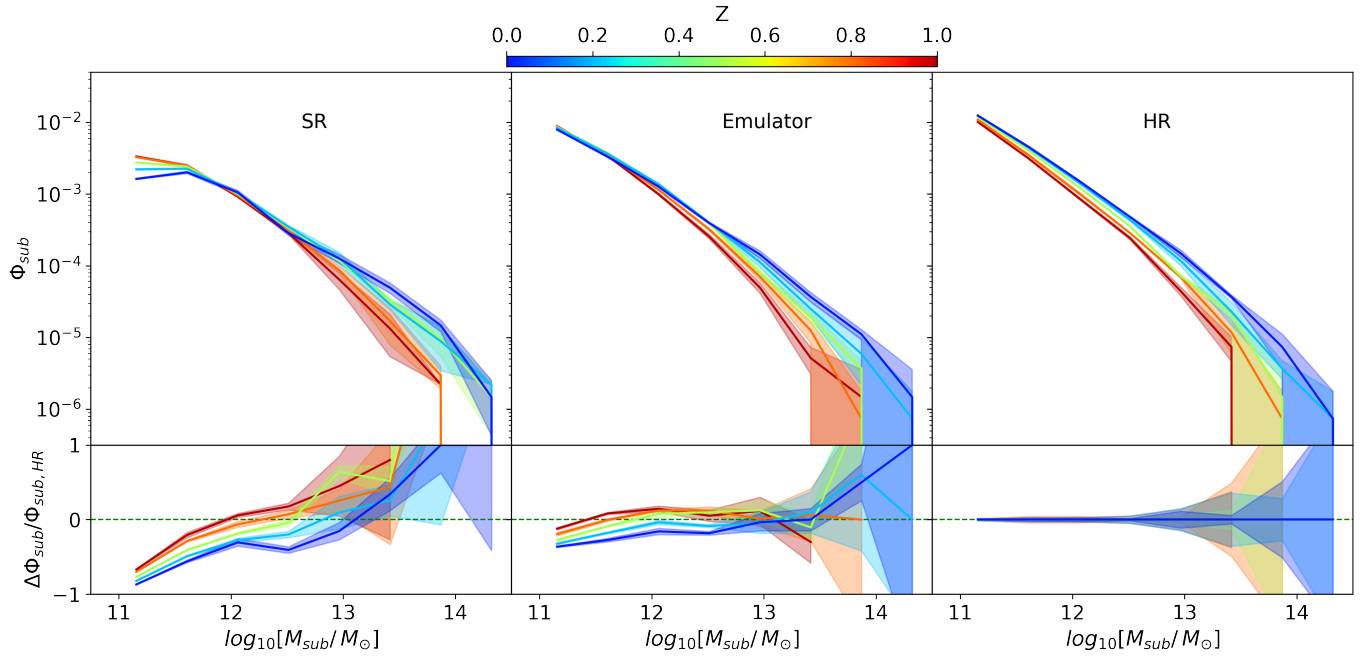


FIG. 6.— The subhalo mass function at redshifts $z = 1, 0.8, 0.5, 0.2, 0$ calculated from the SR, Emulator and HR fields. The color of each curve denotes the redshift of simulation in test set. The shaded areas indicate 1σ standard deviation from all test sets. The upper panel shows halo mass functions and lower panel shows fractional errors.

whether the merger histories of these halos are also consistent the HR run. To do this, we use the merger tree algorithm built into the cosmological N -body code Gadget-4 (Springel et al. 2021), called Hierarchical Bound Tracing (HBT). It uses information from earlier snapshots to help derive the latest halo catalogue. Starting from high redshift, the algorithm identifies main halos at their formation and follows the particles within these halos through subsequent snapshots. This process generates a merger tree for the main halos at the first stage, which

is then extended to include subhalos.

Figure 10 shows a direct visual comparison of merger trees for the same halo selected from the SR field, Emulator output and the HR field (from bottom to top, redshift changes from $z = 1$ to $z = 0$). This halo, with mass $\sim 10^{14} M_\odot$ was selected based on and mass relative to the HR run. The size of each tree node is scaled according to halo mass, with red colors indicating the main progenitors. Although the SR merger tree looks authentic, with mass fluctuations and mergers, the redshifts

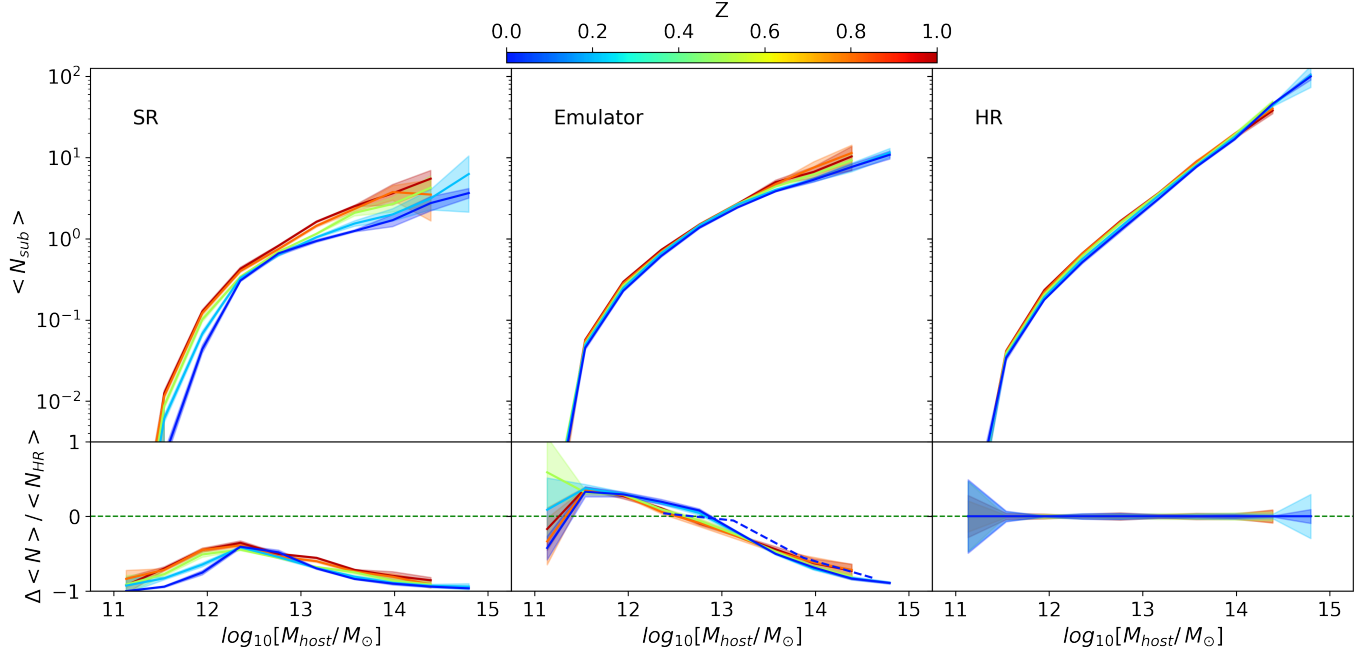


FIG. 7.— The mean occupation number of subhalos vs host halo mass at redshift $z = 1, 0.8, 0.5, 0.2, 0$ measured from the SR, Emulator and HR fields. The y axis is the averaged number of subhalos in each host halo mass bin. The color of each curve corresponds to its redshift according to the color bar at the top. The shaded area shows the 1σ standard deviation from all test sets. The dashed blue line represents the mean occupation number at $z = 0$, calculated by selecting only those halos where 99 percent of their particles lie within a single particle chunk (see text).

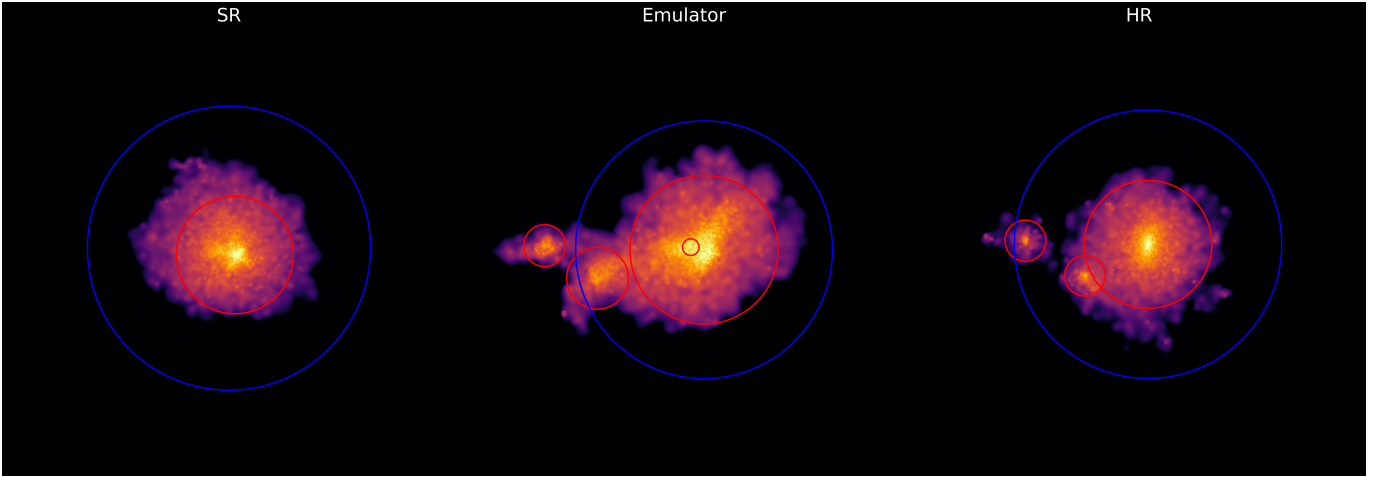


FIG. 8.— Visual comparison of subhalos from SR, Emulator and HR output, centered on a massive halo with halo mass $1.1 \times 10^{13} M_{\odot}$. We mark host halos with blue circles and subhalos with red circles. The radius of the circle is proportional to the virial radius. All halos shown here have mass $> 100 M_{DM}$.

when the mergers happen and their numbers are very different in detail from the counterpart HR halo. In contrast, the Emulator’s merger tree more accurately predicts the redshift and masses involved in the main merger event. The emulator output also features more small-mass halos, i.e., more substructures than the SR field, and places them in relatively correct locations as a function of time.

To further validate the actual merger history, such as mass accretion history measured from the SR, Emulator and HR fields, we select halos within different mass ranges from the SR and emulator fields and calculate the mass error relative to the corresponding HR halos from $z = 1$ to $z = 0$. First, we split all the halos in the HR run at $z = 0$ into four different mass regimes, then track the mass history of each halo along its main progenitor branch from $z = 1$ to $z = 0$. To demonstrate the accuracy of our emulation and SR model, we calculate the

mass error using the following equation:

$$\text{error} = \frac{M_{\text{halo,pred}}}{M_{\text{halo,HR}}} - 1 \quad (16)$$

Figure 11 shows the fractional error in the mass history along the main progenitor branch, calculated from one of our test sets. For halos with masses greater than $10^{13} M_{\odot}$, our SR model captures the mass to within 40% error for the middle 68% percentile, while our Emulator further reduces this margin to within 25%. As we move to lower mass ranges, $[10^{12}, 10^{13}] M_{\odot}$ and $[10^{11}, 10^{12}] M_{\odot}$, the Emulator significantly improves the accuracy of the predicted halo mass. In contrast, the SR model, reflecting the stochastic generation of small-scale structures, has a middle 68% error range 3 ~ 4 times larger than that of the Emulator.

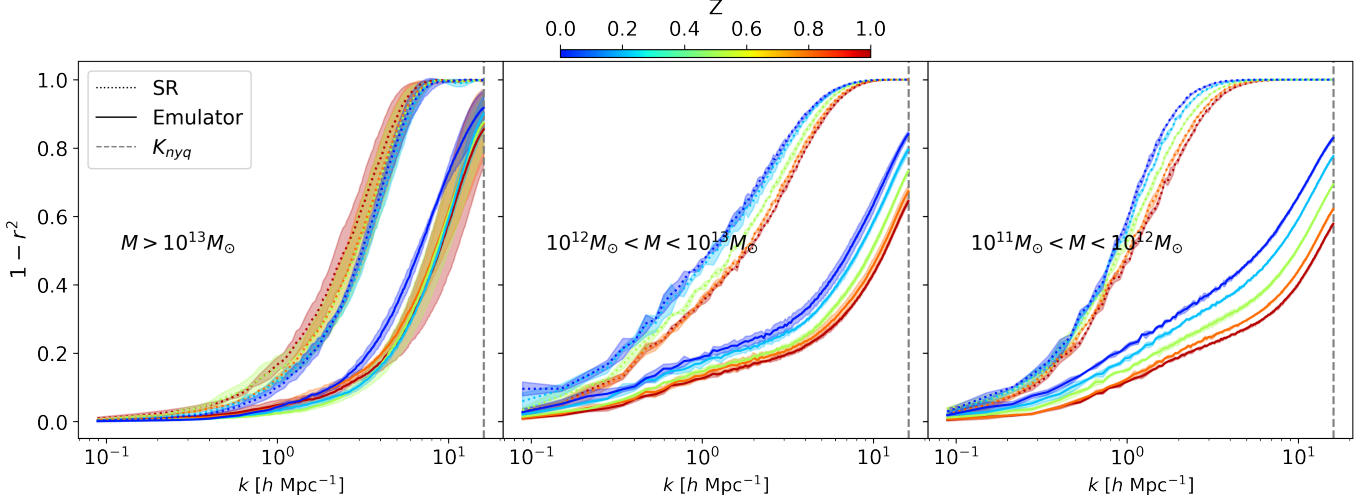


FIG. 9.— The halo cross correlation error for the SR (dotted lines) and Emulator (solid lines) models for different halo mass regimes (panels from left to right). The color of each curve corresponds to its redshift according to the color bar. The shaded area shows the 1σ standard deviation from all test sets. The vertical dashed gray lines indicate the Nyquist frequency.

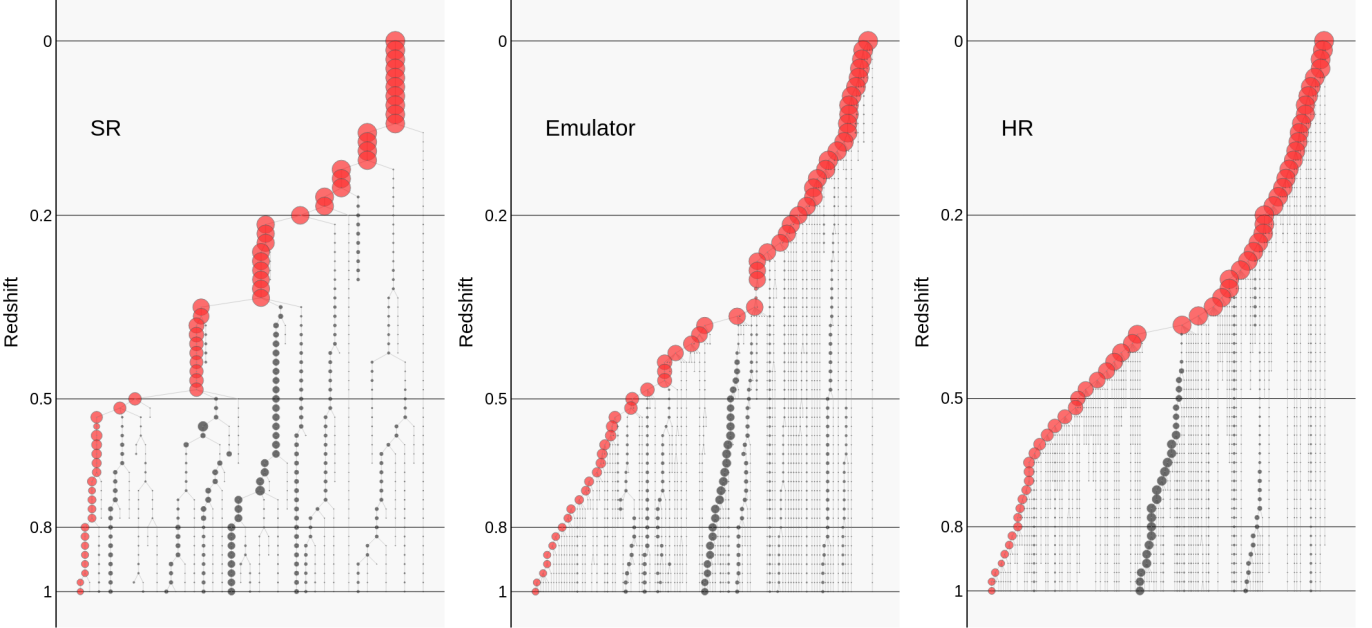


FIG. 10.— Visualization of merger trees for an example halo in the SR, Emulator and HR field at $z = 0$. Time is depicted as progressing from bottom to top, covering the redshift range of $z = 1$ to $z = 0$. The size of each node is scaled with halo mass. Red circles indicate the main progenitor branch.

4. DISCUSSION

The application of SR techniques has been explored in many different works. Some SR models are designed to generate a range of possible HR simulations based on LR inputs, which could be advantageous when many simulations or mock observations are required. However, this approach can be problematic when a specific HR realization with given initial conditions is needed. The model in our current paper addresses this by incorporating information about the particle initial conditions (displacements and velocities) from the high-resolution N -body simulations we are trying to match. In N -body simulation algorithms, once the initial conditions are fixed, the simulation results at different redshifts are also deterministic. These initial conditions provide sufficient information to correct the stochastically generated SR field. Combining the

SR model with our Emulator, we can generate SR fields with different random seeds and adjust them to the desired results by leveraging the initial displacement and velocity.

The accuracy of the refined SR field, adjusted by our Emulator, represents a significant improvement over the initial SR outputs. This improvement was demonstrated through the analysis of Fourier modes in Section 3.2, the halo abundance in Section 3.3.1 and merger histories in Section 3.3.3. As expected, our emulator achieves a much closer correlation with HR field compared to the SR field on scales below the LR resolution, in this case from $k \sim 1 h \text{Mpc}^{-1}$ to the HR model's Nyquist frequency. Additionally, in terms of halo mass function and the mean subhalo occupation number, our Emulator has shown improvement in predicting substructures. We also introduced the "halo cross spectrum", which measures the spatial correlations of halo mass and position, in Section 3.3.2.

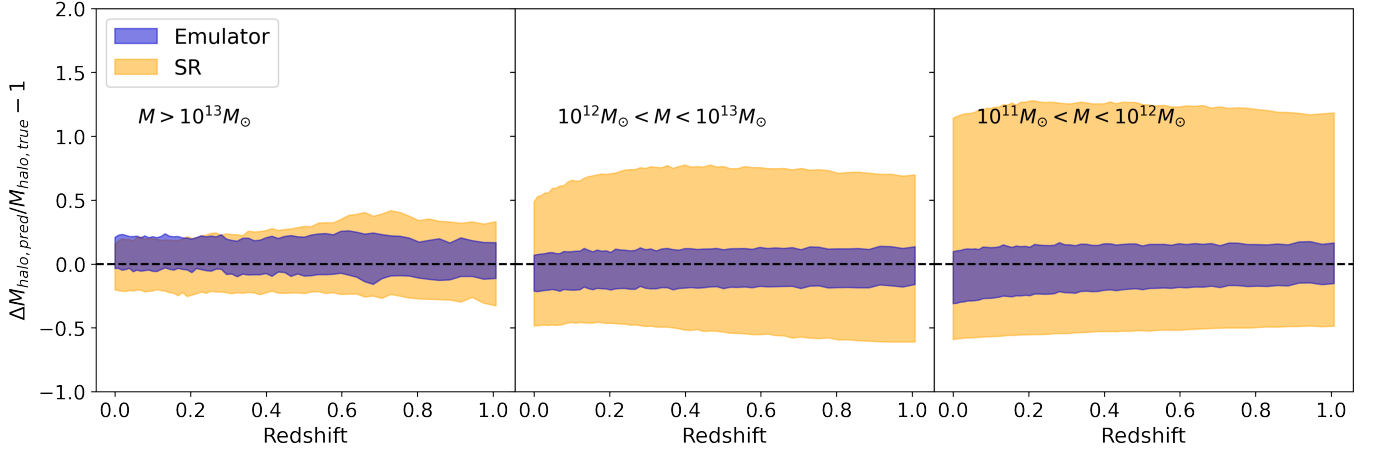


FIG. 11.— The middle 68% percentile error regions of halo mass history along the main progenitor branches of halos in the Emulator (blue) and SR (orange) outputs.

This statistic shows that we have improved this correlation. Furthermore, our emulator successfully predicts accurate halo histories, as demonstrated by comparing merger trees and mass accretion histories with the HR runs.

However, there remain some discrepancies in agreement with the HR runs. Both the SR model and the Emulator currently exhibit a lack of substructures within very massive halos, particularly at the higher mass end, as seen in Figure 7 and the visual comparisons in Section 3.1. Most of the missing halos are of low mass, suggesting that increasing the resolution of the Eulerian fields, used to provide direct information about substructures to the discriminator, could improve this. At the current spatial resolution ($\approx 0.2h^{-1}\text{Mpc}$), the discriminator struggles to identify substructures within massive halos that require higher contrast to resolve.

Another area for future improvement is related to the need to split the entire N -body simulation (with 512^3 particles) into 128^3 chunks due to limited GPU memory. This chunking limits the emulator’s knowledge to correlations and interactions among particles within the same chunk, making it impossible to identify substructures that span multiple chunks. Increasing the chunk size or the resolution of the Eulerian field is challenging, as an increase by a factor of f leads to f^3 times more memory consumption. This limitation motivates us to search for more memory-efficient methods to incorporate information from the entire N -body simulation as well as the density field. Both of these challenges could potentially be mitigated by exploring more advanced neural networks or memory-efficient strategies.

4.1. Running the Emulator output forward with the N -body code

The output of our SR and Emulator runs has the same format as the true N -body simulations. In principle, we can treat them in the same fashion, as we have done for halo finding and calculating merger trees. A particularly interesting test involves passing the emulator output directly to the N -body code and running it forward in time. If the emulator produces dynamically correct structures, we expect the model to evolve reasonably well, approximating the outcome of a full HR simulation at later redshifts. We have conducted an initial test of this approach.

We take the output from our Emulator at an early redshift ($z = 1$) and input it into MP-Gadget to run a forward N -body

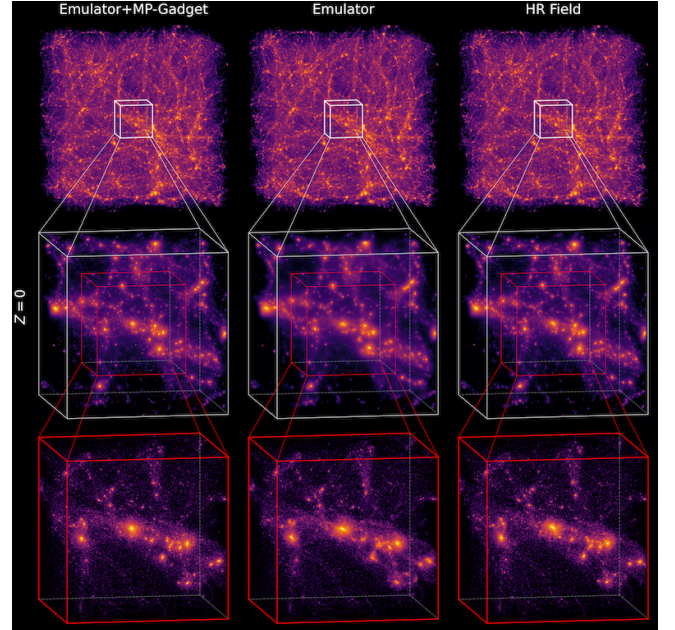


FIG. 12.— 3D visualization of Emulator+MP-Gadget, Emulator model output and HR dark matter density fields with boxsize $100h^{-1}\text{Mpc}$ (first row), $20h^{-1}\text{Mpc}$ (second row), $11h^{-1}\text{Mpc}$ (third row) at $z = 0$

simulation. We then compare the results of this forward simulation with those of an actual HR simulation. The results, shown in Figure 12, demonstrate that this hybrid approach generates more realistic substructures, close to those seen in HR simulations, while still preserving the large-scale structures. This not only validates the accuracy of our model’s predictions but also suggests potential for a hybrid N -body+Emulator method. We plan to explore this further in future work.

5. SUMMARY AND CONCLUSIONS

We have developed and evaluated an emulator based on neural networks that produces super-resolved cosmological N -body simulation outputs. The inputs are a low-resolution N -body simulation and the initial conditions from a high-resolution simulation. The Emulator processes the outputs from the SR model of Zhang et al. 2023, which is based on an LR simulation. By integrating the initial conditions of particles (including initial displacement and velocity), the emulator predicts the adjustments to the SR model’s 6D phase

space output. These adjustments ensure that emulator's output closely aligns with the HR N -body simulation using the same initial conditions.

We conducted detailed validation of our Emulator by comparing various statistics calculated from test sets. In Section 3.1, we presented a visual comparison between the SR model, the Emulator and the corresponding HR simulation. These comparisons demonstrate that on large scales, the SR, emulator and HR fields appear identical. While SR field presents visually convincing small-scale structures, it differs in detail from the HR simulations. However, the Emulator output successfully aligns with the HR simulation even on scales well below the resolution of the LR simulation.

In Section 3.2, we examined the outputs in Fourier space and found that the emulator output correlates much more closely with the HR field than SR output, from $k = 1h\text{Mpc}^{-1}$ down to the Nyquist frequency. The Emulator's accuracy represents a significant improvement over the SR field. To evaluate the halo population and substructures, we compute the halo and subhalo mass functions, as well as mean occupation number, in Section 3.3. Both the SR and Emulator host halo mass abundance have good statistical agreement with HR, showing our emulator does not diminish the previous results from SR field (Zhang et al. 2023). At the same time, the subhalo mass function shows that the Emulator output improves significantly over the SR field, adjusting the SR field to the HR field and improving the prediction of small-scale structures. However, a deficit in the subhalo abundance for halos of mass $[10^{13}, 10^{14}] M_{\odot}$ indicates that current model still struggles to predict a sufficient number of substructures within large mass halos, likely due to the limitations of the Eulerian field resolution.

To quantify the correlation of halo properties (position and mass) between the Emulator and HR field, we introduced a "halo cross spectrum" to evaluate this in Fourier space. In Section 3.3.2, we show that our emulator output leads to significant improvement over SR in the halo mass regime $> 10^{11} M_{\odot}$. Additionally, in Section 10, we validate the emulator's performance over time by visually comparing the merger trees of a massive halo from the SR, Emulator and HR fields. We find that the emulator successfully corrects the merger history compared to the SR result.

Our findings demonstrate the emulator's capability to adjust the SR field output to match the corresponding HR field by utilizing the initial conditions. Our Emulator serves as a promising foundation for emulating N -body simulations under different constraints, suggesting the feasibility of generally emulating outputs for simulations with varying cosmological parameters across a wide range of redshifts. The integration of the SR model with the emulator framework enables the rapid and accurate generation of results across various redshifts, providing an effective tool which can compete with other approximate methods such as those of Feng et al. (2016) and Scoccimarro & Sheth (2002), but promising more accuracy and the potential inclusion of more physics. The emulator approach allows for the generation of mock halo catalogs, as well as other non-linear statistics (such as computing power spectrum covariance matrices), and should become a useful tool for facilitating the constraint of cosmological parameters from cosmological surveys.

DATA AVAILABILITY

The model framework is based on map2map <https://github.com/eelregit/map2map>. This PyTorch-based

framework is a general-purpose tool for transforming field data. The trained model weights and the pipeline to generate the fields will be available at (<https://github.com/xwzhang98/SREmulator>). Training and test sets data generated in this work will be shared on reasonable request to the corresponding author.

ACKNOWLEDGEMENTS

This research is part of the Frontera computing project at the Texas Advanced Computing Center. Frontera is made possible by NSF award OAC-1818253. TDM acknowledges funding from NASA ATP 19-ATP19-0084 and 80NSSC20K0519. TDM and RACC also acknowledge funding from NASA ATP 80NSSC18K101, and NASA ATP NNX17AK56G. SB was supported by NASA ATP 80NSSC22K1897. This work and AD's participation was also supported by the NSF AI Institute: Physics of the Future, NSF PHY-2020295. The computational results presented have been achieved using Vera at Pittsburgh Supercomputing Center (PSC). This work also used Anvil at Purdue University through allocation PHY240032 from the Advanced Cyberinfrastructure Coordination Ecosystem: Services & Support (ACCESS) program, which is supported by National Science Foundation grants 2138259, 2138286, 2138307, 2137603, and 2138296. We also acknowledge the code packages used in this work: The model framework is based on map2map <https://github.com/eelregit/map2map>. The simulations for training and testing is run with MP-Gadget (<https://github.com/MP-Gadget/MP-Gadget>). Visualization in this work is performed with open source code gaepsi2 (<https://github.com/rainwoodman/gaepsi2>) and plotly (Inc. 2015). Data and catalog analysis in this work is performed with open-source software PyTorch (Paszke et al. 2019), nbodyskit (Hand et al. 2018) and ytree (Smith & Lang 2019).

APPENDIX

RESULTS FROM TRAINING THE EMULATOR WITHOUT DISCRIMINATOR GUIDANCE

We now present the results of training the same Emulator without discriminator guidance. In this context, "without discriminator guidance" means training the neural network using the loss function in Equation 6, but without the third adversarial term.

Figure 13 shows the result from the Emulator without discriminator guidance (hereafter referred to as Emulator w/o DG). The first row shows the whole $(100h^{-1}\text{Mpc})^3$ volume, centered on the same halo as in Figure 2 and Figure 3, to show the large-scale structures, the second row and the third row shows a sub-volume of $(20h^{-1}\text{Mpc})^3$ and $(11h^{-1}\text{Mpc})^3$, to show the different detailed structures and halo distributions. Comparing with Figure 2 and Figure 3, we can see that the Emulator w/o DG still appears authentic on large scales, similar to our Emulator+DG model. However, as shown in the third column, on smaller scales, the Emulator w/o DG tends to create a much smoother density field, resulting in a lack of substructures.

Figure 14 shows the results of stochasticity, calculated using the same equations as in Section 3.2. Comparing these results with those in Figure 4, we can see that the Emulator w/o DG performs slightly better in the density field and produces comparable results in displacement and momentum.

The host-halo mass function, sub-halo mass function, and mean occupation number for the Emulator w/o DG's output are shown in Figure 15. Both the host-halo and sub-halo mass functions show a deficit in the lower mass region, indicating that training without discriminator guidance (DG) lacks the detailed structures observed on smaller scales in the Emulator+DG model. Additionally, the mean occupation number reveals that training without DG results in fewer low-mass

subhalos within the range of $[10^{11}, 10^{13}] M_{\odot}$.

Overall we have therefore seen that the discriminator part of the emulator is necessary to produce distinct substructures and a realistic density field. Without it the emulator does have slightly more accurate Fourier modes but it has a significantly smoother density field on halo scales. We therefore have decided to include the discriminator in the fiducial version of the emulator (used in the main body of the paper).

REFERENCES

- Aarseth S. J., 1963, *MNRAS*, **126**, 223
- Alves de Oliveira R., Li Y., Villaescusa-Navarro F., Ho S., Spergel D. N., 2020, *NeurIPS 2020 Machine Learning and the Physical Sciences Workshop*
- Bagla J. S., 2002, *Journal of Astrophysics and Astronomy*, **23**, 185
- Barron J. T., 2017, *arXiv e-prints*, p. arXiv:1701.03077
- Berger P., Stein G., 2019, *MNRAS*, **482**, 2861
- Bernardini M., Mayer L., Reed D., Feldmann R., 2020, *MNRAS*, **496**, 5116
- Bird S., Ni Y., Di Matteo T., Croft R., Feng Y., Chen N., 2022, *MNRAS*, **512**, 3703
- Brock A., Donahue J., Simonyan K., 2018, *arXiv e-prints*, p. arXiv:1809.11096
- Crocce M., Pueblas S., Scoccimarro R., 2006, *MNRAS*, **373**, 369
- Dai B., Seljak U., 2021, *Proceedings of the National Academy of Science*, **118**, 2020324118
- Davé R., Anglés-Alcázar D., Narayanan D., Li Q., Rafieferantsoa M. H., Appleby S., 2019, *MNRAS*, **486**, 2827
- Dvorkin C., et al., 2022, *arXiv e-prints*, p. arXiv:2203.08056
- Elfwing S., Uchibe E., Doya K., 2017, *arXiv e-prints*, p. arXiv:1702.03118
- Feng Y., Chu M.-Y., Seljak U., McDonald P., 2016, *MNRAS*, **463**, 2273
- Goodfellow I. J., Pouget-Abadie J., Mirza M., Xu B., Warde-Farley D., Ozair S., Courville A., Bengio Y., 2014, *arXiv e-prints*, p. arXiv:1406.2661
- Hand N., Feng Y., Beutler F., Li Y., Modi C., Seljak U., Slepian Z., 2018, *AJ*, **156**, 160
- He S., Li Y., Feng Y., Ho S., Ravanbakhsh S., Chen W., Póczos B., 2019, *Proceedings of the National Academy of Science*, **116**, 13825
- Heitmann K., et al., 2008, *Computational Science and Discovery*, **1**, 015003
- Hinshaw G., et al., 2013, *ApJS*, **208**, 19
- Ho J., Jain A., Abbeel P., 2020, *arXiv e-prints*, p. arXiv:2006.11239
- Hopkins P. F., Kereš D., Oñorbe J., Faucher-Giguère C.-A., Quataert E., Murray N., Bullock J. S., 2014, *MNRAS*, **445**, 581
- Inc. P. T., 2015, Collaborative data science, <https://plot.ly>
- Jamieson D., Li Y., de Oliveira R. A., Villaescusa-Navarro F., Ho S., Spergel D. N., 2023, *ApJ*, **952**, 145
- Johnson J., Alahi A., Fei-Fei L., 2016, *arXiv e-prints*, p. arXiv:1603.08155
- Kodi Ramanah D., Charnock T., Villaescusa-Navarro F., Wandelt B. D., 2020a, *MNRAS*, **495**, 4227
- Kodi Ramanah D., Charnock T., Villaescusa-Navarro F., Wandelt B. D., 2020b, *MNRAS*, **495**, 4227
- Lesgourgues J., 2011, *arXiv e-prints*, p. arXiv:1104.2932
- Li Y., Ni Y., Croft R. A. C., Di Matteo T., Bird S., Feng Y., 2021, *Proceedings of the National Academy of Science*, **118**, e2022038118
- Liu L., Jiang H., He P., Chen W., Liu X., Gao J., Han J., 2019, *arXiv e-prints*, p. arXiv:1908.03265
- Maksimova N. A., Garrison L. H., Eisenstein D. J., Hadzhiyska B., Bose S., Satterthwaite T. P., 2021, *Monthly Notices of the Royal Astronomical Society*, **508**, 4017
- Modi C., Feng Y., Seljak U., 2018, *J. Cosmology Astropart. Phys.*, **2018**, 028
- Ni Y., Li Y., Lachance P., Croft R. A. C., Di Matteo T., Bird S., Feng Y., 2021, *MNRAS*, **507**, 1021
- Ni Y., et al., 2022, *MNRAS*, **513**, 670
- Paszke A., et al., 2019, *arXiv e-prints*, p. arXiv:1912.01703
- Perraudin N., Srivastava A., Lucchi A., Kacprzak T., Hofmann T., Réfrégier A., 2019, *Computational Astrophysics and Cosmology*, **6**, 5
- Perraudin N., Marcon S., Lucchi A., Kacprzak T., 2020, *arXiv e-prints*, p. arXiv:2004.08139
- Rodríguez A. C., Kacprzak T., Lucchi A., Amara A., Sgier R., Fluri J., Hofmann T., Réfrégier A., 2018, *Computational Astrophysics and Cosmology*, **5**, 4
- Ronneberger O., Fischer P., Brox T., 2015, *arXiv e-prints*, p. arXiv:1505.04597
- Rouhiainen A., Gira M., Münchmeyer M., Lee K., Shiu G., 2023, *arXiv e-prints*, p. arXiv:2311.05217
- Saharia C., Chan W., Chang H., Lee C. A., Ho J., Salimans T., Fleet D. J., Norouzi M., 2021, *arXiv e-prints*, p. arXiv:2111.05826
- Schanz A., List F., Hahn O., 2023, *arXiv e-prints*, p. arXiv:2310.06929
- Scoccimarro R., Sheth R. K., 2002, *MNRAS*, **329**, 629
- Sipp M., LaChance P., Croft R., Ni Y., Di Matteo T., 2023, *MNRAS*, **525**, 1807
- Smith B., Lang M., 2019, *The Journal of Open Source Software*, **4**, 1881
- Smith M. J., Geach J. E., Jackson R. A., Arora N., Stone C., Courteau S., 2022, *Monthly Notices of the Royal Astronomical Society*, **511**, 1808
- Sohl-Dickstein J., Weiss E. A., Maheswaranathan N., Ganguli S., 2015, *arXiv e-prints*, p. arXiv:1503.03585
- Springel V., White S. D. M., Tormen G., Kauffmann G., 2001, *MNRAS*, **328**, 726
- Springel V., et al., 2018, *MNRAS*, **475**, 676
- Springel V., Pakmor R., Zier O., Reinecke M., 2021, *MNRAS*, **506**, 2871
- Tröster T., Ferguson C., Harnois-Déraps J., McCarthy I. G., 2019, *MNRAS*, **487**, L24
- Villaescusa-Navarro F., et al., 2020, *arXiv e-prints*, p. arXiv:2010.00619
- Wadekar D., Villaescusa-Navarro F., Ho S., Perreault-Levasseur L., 2020, *arXiv e-prints*, p. arXiv:2007.10340
- Wang Z., Chen J., Hoi S. C. H., 2019, *arXiv e-prints*, p. arXiv:1902.06068
- Wu Y., He K., 2018, *arXiv e-prints*, p. arXiv:1803.08494
- Yue L., Shen H., Li J., Yuan Q., Zhang H., Zhang L., 2016, *Signal Processing*, **128**
- Zel'dovich Y. B., 1970, *A&A*, **5**, 84
- Zhang X., Wang Y., Zhang W., Sun Y., He S., Contardo G., Villaescusa-Navarro F., Ho S., 2019, *arXiv e-prints*, p. arXiv:1902.05965
- Zhang X., Lachance P., Ni Y., Li Y., Croft R. A. C., Di Matteo T., Bird S., Feng Y., 2023, *arXiv e-prints*, p. arXiv:2305.12222
- von Hoerner S., 1960, *ZAp*, **50**, 184

arXiv, making the reviewing process simpler for authors and referees alike. Learn more at <http://astro.theoj.org>.

This paper was built using the Open Journal of Astrophysics \LaTeX template. The OJA is a journal which provides fast and easy peer review for new papers in the astro-ph section of the

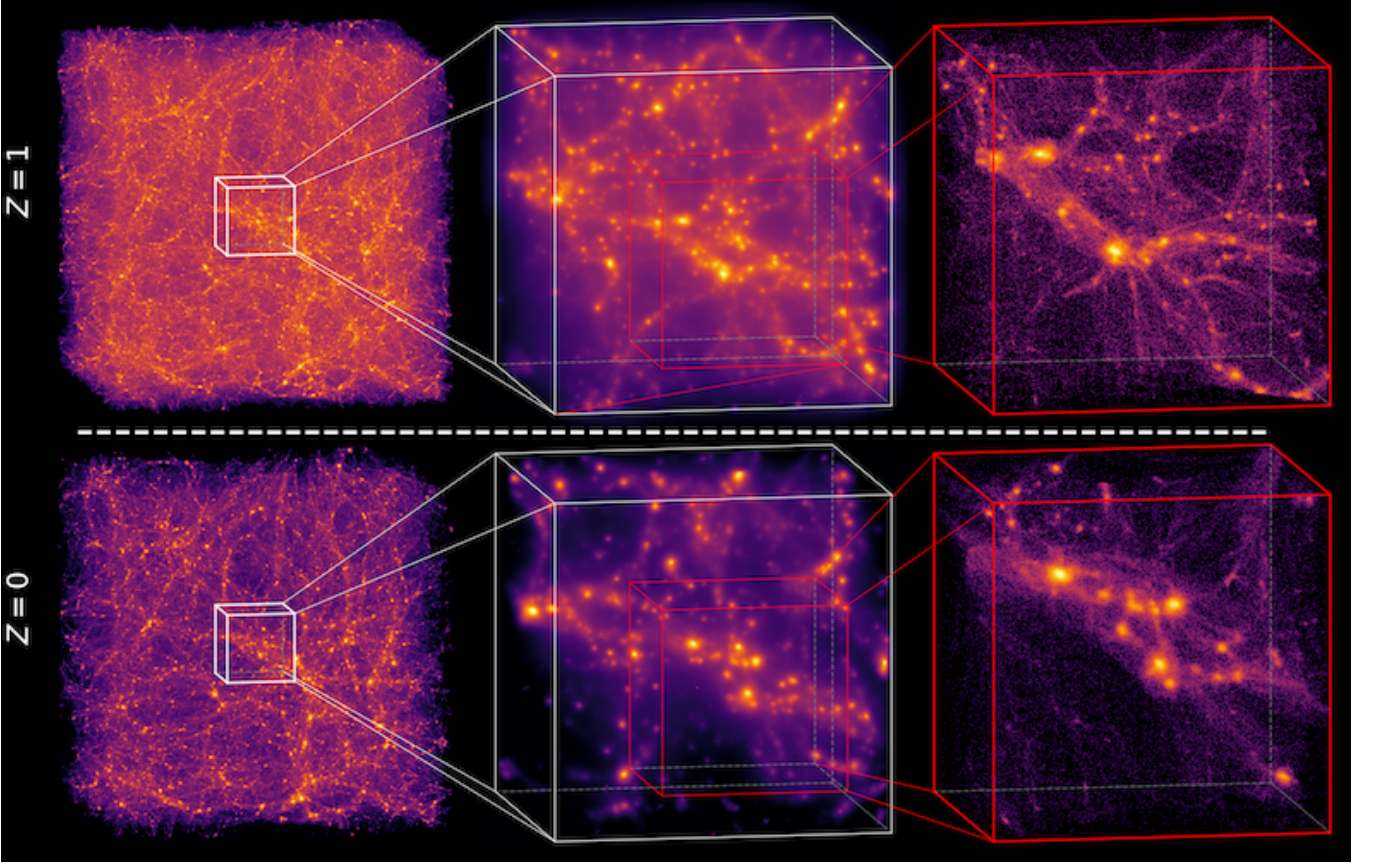


FIG. 13.— 3D visualization of the Emulator w/o DG density fields with boxsize $100h^{-1}\text{Mpc}$ (first column), $20h^{-1}\text{Mpc}$ (second column), $11h^{-1}\text{Mpc}$ (third column) at $z = 1$ and $z = 0$.

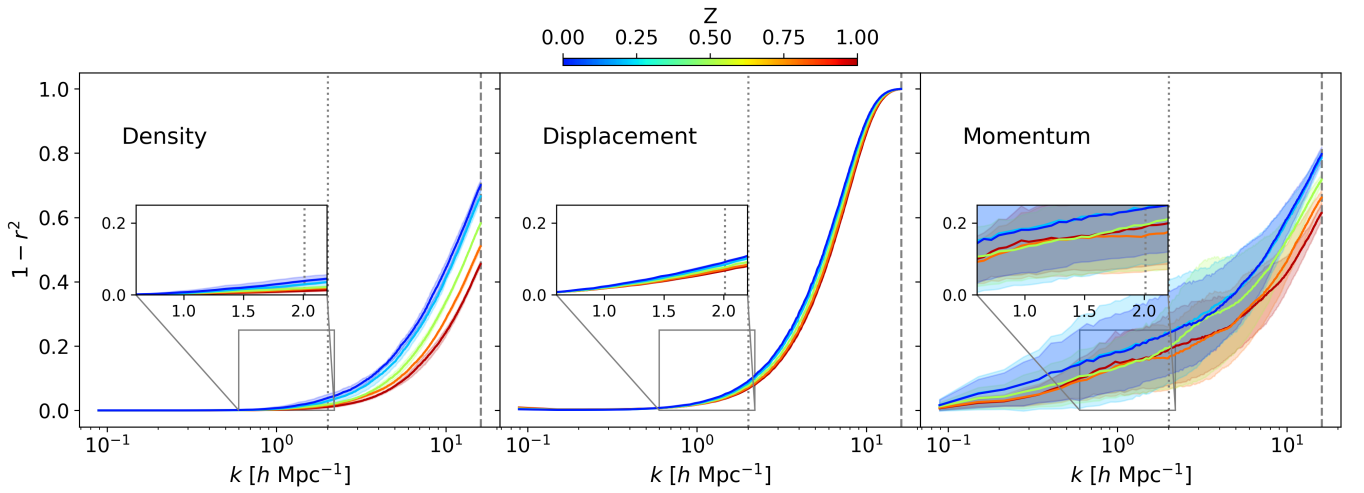


FIG. 14.— Stochasticity of individual Fourier modes as a function of wavenumber. The color of each curve corresponds to its redshift according to the color bar. The shaded area shows the 1σ standard deviation from all test sets. The vertical dashed gray line indicates the Nyquist frequency of HR simulation and the dotted gray line is the Nyquist frequency of the LR simulation.

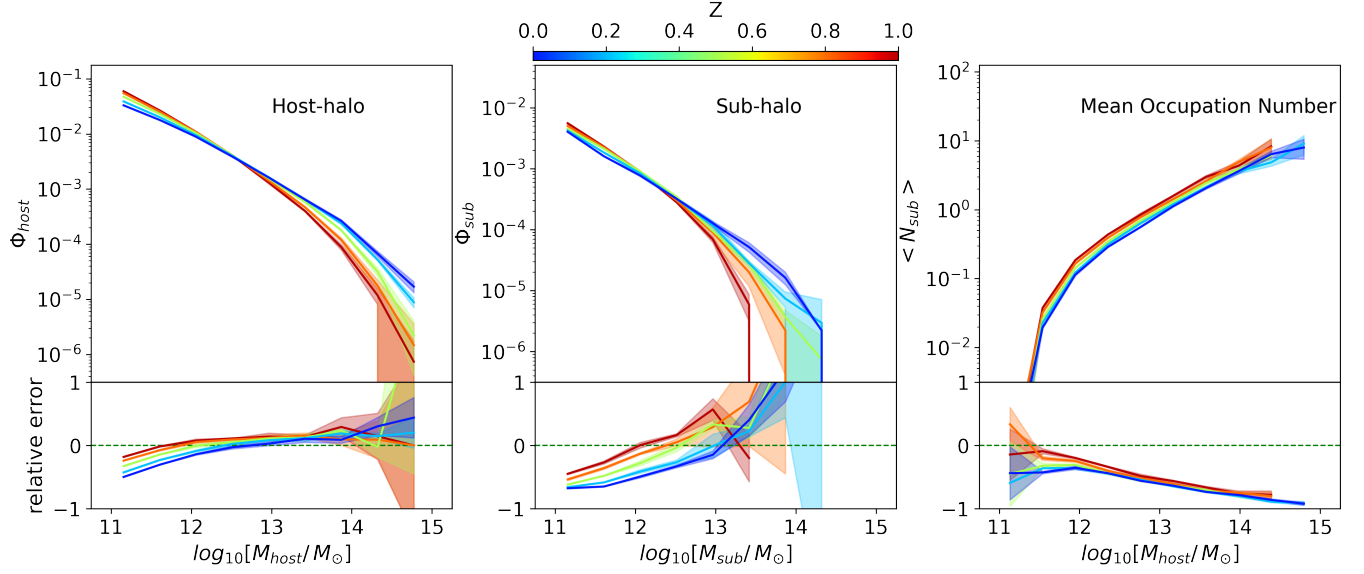


FIG. 15.— The host halo, subhalo mass function and mean occupation number at redshifts $z = 1, 0.8, 0.5, 0.2, 0$ measured from the Emulator w/o DG output. The color of each curve denotes the redshift of simulation in test set. The shaded areas indicate 1σ standard deviation from all test sets. The upper panel shows halo mass functions and lower panel shows fractional errors